Remote Sensing of Environment 112 (2008) 3055-3063

Contents lists available at ScienceDirect

Remote Sensing of Environment

journal homepage: www.elsevier.com/locate/rse

Active fire detection and characterization with the advanced spaceborne thermal emission and reflection radiometer (ASTER)

Louis Giglio [a,b,*], Ivan Csiszar [b], Ágoston Restás [c], Jeffrey T. Morisette [d], Wilfrid Schroeder [b], Douglas Morton [b], Christopher O. Justice [b]

[a] Science Systems and Applications, Inc., Lanham, Maryland, USA
[b] Department of Geography, University of Maryland, College Park, Maryland, USA
[c] Szendrő Fire Department, Szendrő, Hungary
[d] NASA Goddard Space Flight Center, Greenbelt, Maryland, USA

ARTICLE INFO

Article history:
Received 16 October 2007
Received in revised form 26 February 2008
Accepted 1 March 2008

Keywords:
Biomass burning
Fire detection
Fire radiative power
ASTER
MODIS

ABSTRACT

We present an automated fire detection algorithm for the Advanced Spaceborne Thermal Emission and Reflection Radiometer (ASTER) sensor capable of mapping actively burning fires at 30-m spatial resolution. For daytime scenes, our approach uses near infrared and short-wave infrared reflectance imagery. For nighttime scenes a simple short wave infrared radiance threshold is applied. Based on a statistical analysis of 100 ASTER scenes, we established omission and commission error rates for nine different regions. In most regions the probability of detection was between 0.8 and 0.9. Probabilities of false alarm varied between 9×10^{-8} (India) and 2×10^{-5} (USA/Canada). In most cases, the majority of false fire pixels were linked to clusters of true fire pixels, suggesting that most false fire pixels occur along ambiguous fire boundaries. We next consider fire characterization, and formulate an empirical method for estimating fire radiative power (FRP), a measure of fire intensity, using three ASTER thermal infrared channels. We performed a preliminary evaluation of our retrieval approach using four prescribed fires which were active at the time of the Terra overpass for which limited ground-truth data were collected. Retrieved FRP was accurate to within 20%, with the exception of one fire partially obscured by heavy soot.

1. Introduction

At present a number of satellite-based active fire, or "hot spot", data products are available for operational and experimental use. The number of sensors from which these data sets are derived has grown considerably over the past decade, and now includes the Advanced Very High Resolution Radiometer (AVHRR), the Moderate Resolution Imaging Spectroradiometer (MODIS), the Along-Track Scanning Radiometer (ATSR) and Advanced Along-Track Scanning Radiometer (AATSR), the Visible and Infrared Scanner (VIRS), the Geostationary Operational Environmental Satellite (GOES) Imager, the Operational Linescan System (OLS), and the Spinning Enhanced Visible and Infrared Imager (SEVIRI) (Arino & Rosaz, 1999; Elvidge et al., 1996; Giglio et al., 2003; Justice et al., 1996, 2002; Prins et al., 2001; Roberts and Wooster, 2007; Stroppiana et al., 2000) While a variety of intercomparisons between satellite-based active fire data sets (or between the fire detection approach associated with each) have been performed (Li et al., 2001; Ichoku et al., 2003), there has been little rigorous product validation. The primary reason for this arises from the dynamic nature of fire and the short time scales over which it interacts with, and moves across, the landscape. Continued interest exists, therefore, in using high resolution sensors on board aircraft or satellites to provide spatially and temporally coincident fire imagery. The resulting fire "snapshots" could then be used to derive detailed, instantaneous maps of fire extent (and perhaps properties) to support validation. In addition, high resolution fire maps are independently useful for ecological field studies on fire and its effects, especially in heterogeneous landscapes and at the wildland–urban interface.

A high-resolution sensor that has facilitated fire validation in recent years is the Advanced Spaceborne Thermal Emission and Reflection Radiometer (ASTER), a 14-channel imaging radiometer on board the National Aeronautics and Space Administration's (NASA) Terra satellite. Since ASTER co-resides with the Terra MODIS instrument, high resolution ASTER fire masks have become an important tool in the ongoing validation of the 1-km Terra MODIS active fire products initiated by Morisette et al. (2005a,b) and Csiszar et al. (2006). Since manual production of fire masks is time consuming, and simple fixed threshold methods do not scale well (both spatially and temporally), a consistent, automated source of ASTER fire masks is desirable. In this paper we present a fire detection algorithm that uses ASTER observations to provide binary "yes/no" fire masks at 30-m spatial resolution.

* Corresponding author. Science Systems and Applications, Inc., Lanham, Maryland, USA.
E-mail address: louis_giglio@ssaihq.com (L. Giglio).

0034-4257/$ – see front matter © 2008 Elsevier Inc. All rights reserved.
doi:10.1016/j.rse.2008.03.003

Table 1
ASTER channel characteristics

Band Number	Central Wavelength (μm)	Spatial Resolution
1	0.56	15 m
2	0.66	
3N	0.82	
3B	0.82	
4	1.65	30 m
5	2.17	
6	2.21	
7	2.26	
8	2.33	
9	2.40	
10	8.30	90 m
11	8.65	
12	9.10	
13	10.60	
14	11.30	

Algorithm performance is evaluated using 100 ASTER scenes for which fire pixels were manually identified. We next consider the potential of ASTER for fire characterization, and present an empirical method for retrieving fire radiative power (FRP), a measure of fire intensity, using ASTER data. The method is then evaluated using ground truth data obtained for several prescribed fires.

2. The ASTER instrument

The ASTER is a 14-channel imaging radiometer with separate visible and near-infrared (VNIR), short wave infrared (SWIR), and thermal infrared (TIR) optical subsystems (Yamaguchi et al., 1998). The individual subsystems contain four (VNIR), six (SWIR), and five (TIR) spectral bands at 15, 30, and 90 m spatial resolution, respectively. The ASTER band numbering and spectral locations are listed in Table 1. The VNIR and SWIR bands have three and four individually-selectable gain settings, respectively, referred to as *high*, *normal*, *low-1*, and *low-2* (SWIR only). The imaging swath for all bands spans 60 km. Due to various hardware, power, and data storage and download rate constraints, ASTER does not continuously acquire data, but is instead operated on a prioritized acquisition schedule (Yamaguchi et al., 1998).

3. Data

For this study we used 196 radiometrically calibrated and geometrically coregistered Level 1B ASTER scenes acquired between early 2001 and late 2004 for algorithm testing and evaluation. Scene locations and acquisition dates were selected based on current knowledge of the global distribution of fire activity. The locations of all scenes are shown in Fig. 1.

4. Fire detection

4.1. Band selection

Satellite-based fire detection has traditionally relied upon bands located near 4 μm to exploit the high levels of black-body radiation emitted at typical fire temperatures in this region of the electromagnetic spectrum. This region is, in fact, near-optimal for satellite-based fire detection in daytime imagery. This can be seen by considering the ratio R of black-body radiation emitted by a fire (L_{fire}) to the radiance of the ambient non-fire land surface (L_{land}):

$$R = L_{\text{fire}}/L_{\text{land}}. \tag{1}$$

The land radiance is composed of reflected solar radiation and thermal black-body radiation. For now we consider a simplified case of a Lambertian grey-body surface, unit fire emissivity, and no atmosphere. With the Sun located directly overhead, the ratio in Eq. (1) is given by

$$R(\lambda) = \frac{B(\lambda, T_{\text{fire}})}{\rho B(\lambda, T_{\text{sun}})\Omega_{\text{sun}}/\pi + (1-\rho)B(\lambda, T_{\text{land}})} \tag{2}$$

where $B(\lambda, T)$ is the Planck function, ρ is the land surface reflectance, T_{land} is the land surface temperature, and Ω_{sun} is the solid angle subtended by the Sun. The Planck function, which describes the spectral radiance emitted at wavelength λ by a black-body at temperature T, is given by

$$B(\lambda, T) = c_1\lambda^{-5}\left[\exp\left(\frac{c_2}{\lambda T}\right) - 1\right]^{-1} \tag{3}$$

where c_1 and c_2 are constants. In Fig. 2, the ratio $R(\lambda)$ is shown for representative flaming (~1000 K) and smoldering (~600 K) fires. Sensitivity peaks near 4 μm for both cases.

Among the most egregious of the simplifications we have made is the assumption of a grey body surface. In reality, of course, surface reflectance varies considerably with wavelength, and the constant ρ appearing in Eq. (2) should be replaced with the function $\rho(\lambda)$. If we were to substitute the reflectance spectrum of most natural terrestrial components into Eq. (2), the general shape of the curve in Fig. 2 would still resemble that of the ideal case, and peak sensitivity would remain near 4 μm. In contrast, including the atmosphere (which we have

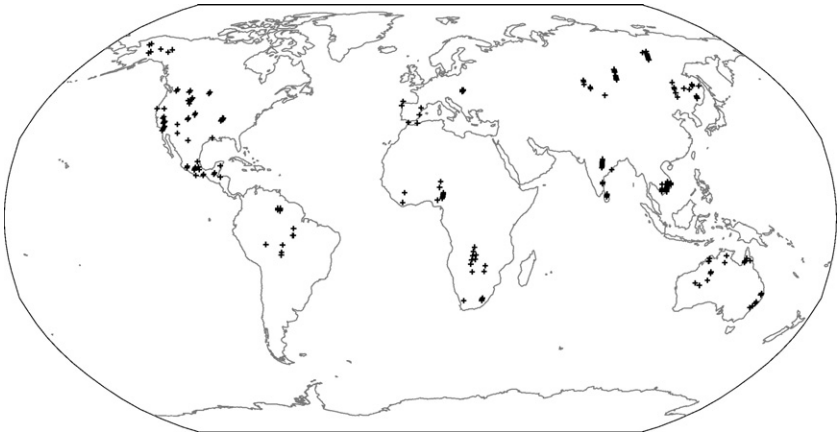

Fig. 1. Locations of the 196 ASTER scenes used in this study.

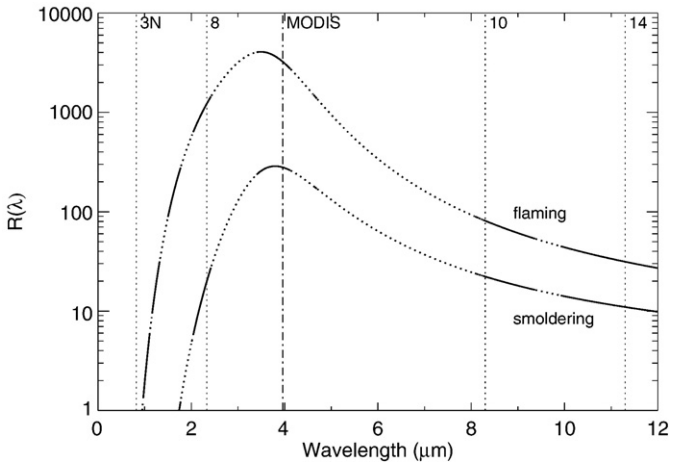

Fig. 2. Ratio *R* of typical fire radiance to typical land surface radiance, as a function of wavelength, for 1000 K flaming and 600 K smoldering fires. The solid portions of both curves denote the locations of atmospheric windows computed using the MODTRAN 4 atmospheric model for the U.S. 1976 standard atmosphere (rural 23 km visibility). This is a highly idealized case with the land surface assumed to be a grey body of 15% reflectance, and no atmospheric extinction. Vertical dotted lines indicate locations of ASTER bands 3N, 8, 10, and 14. Vertical dot-dashed line indicates location of MODIS middle infrared fire bands for comparison.

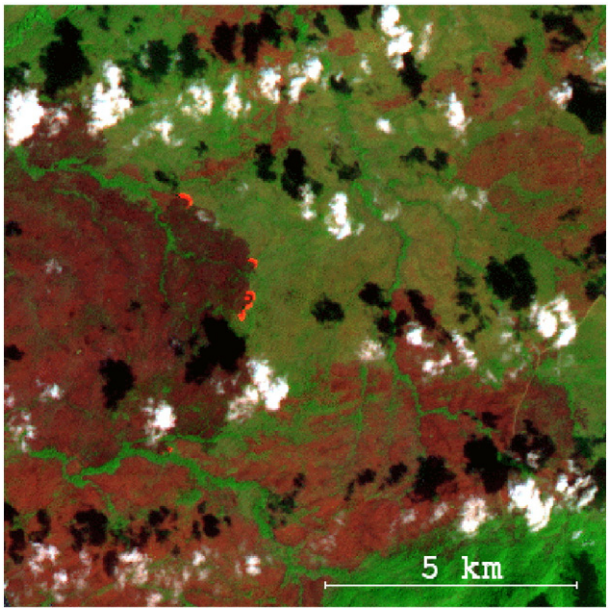

Fig. 3. False color ASTER image of an active fire in eastern Cambodia, acquired 15 January 2003, 03:31 UTC, with band 8 shown as red, band 3N shown as green, and band 1 shown as blue. With this color scheme active fires appear bright red, burn scars appear brown, clouds appear white, and cloud shadows appear black. Approximate location of this fire is 13.2°N, 107.7°E.

heretofore neglected) introduces severe constraints on band selection. Water vapor absorption, for example, renders the spectral region from 5.5 to 7 μm completely useless for observing the terrestrial surface. The locations of atmospheric windows are indicated in Fig. 2 as the solid portions of the curves; the broken portions indicate those spectral regions not usable for surface observation (defined here somewhat arbitrarily as regions in which the atmospheric transmittance is less than 0.6). Conveniently, an atmospheric window exists between 3.6 and 4.1 μm, leaving a wavelength interval located at approximately 4 μm optimal for daytime fire detection.

Since ASTER lacks a 4 μm band, the next best choice would normally be band 9 (2.40 μm). This was the band used by Morisette et al. (2005a) to validate the MODIS fire product in southern Africa, where it was found to work well. Active fires were detected within ASTER scenes by means of a fixed 6.33 W m^{-2} sr^{-1} μm^{-1} threshold criterion applied to band 9 radiance imagery. The authors include a qualitative discussion on the merits of using this particular band in the context of fire detection. There are several issues, however, which complicate the use of band 9 for routine use. In general, all of the ASTER SWIR bands, particularly band 9, can exhibit blooming when pushed to the point of saturation, making it difficult to demarcate actual fire front boundaries. Second, a small number of "dead" pixels having a digital count near zero tend to occur along an edge (or sometimes within) clusters of saturated SWIR pixels, and occurs most often in band 9. These issues were first noted by Morisette et al. (2005a). A third complication is that crosstalk from band 4 spills primarily into bands 5 and 9. While the magnitude of this effect is usually small (Iwasaki et al., 2002), for certain combinations of "mismatched" SWIR-band gain settings (e.g., band 4 *normal*, band 9 *low-2*) the crosstalk will produce a major signal bias in band 9. For the ASTER scenes used in this study, this bias varied between 0.3 and 0.7 in terms of reflectance.

Using Fig. 2 it might be argued that band 10 (8.30 μm) would actually be a superior choice for detecting smoldering fires. While true for pixels that are comparable in size to ASTER's 30-m SWIR bands, the lower 90-m spatial resolution of the TIR bands leaves them significantly less sensitive to fires. A good example of this may be found in Morisette et al. (2005a).

For the reasons discussed above we have selected band 8 (2.33 μm) as the most useful for fire detection. Our approach for daytime scenes in fact uses two ASTER bands, one of which is sensitive to the blackbody radiation emitted by fires (band 8), and another which is insensitive to such radiation but that provides a highly correlated reflectance over "normal" (non-fire) components of terrestrial scenes, which includes soil, vegetation, clouds, and urban areas. The only viable candidate is band 3N (0.82 μm) which, of the four VNIR bands, is the least susceptible to scattering by smoke and other aerosols. Fig. 3 shows a false color band 1, band 3N, and band 8 image of an active fire in eastern Cambodia. In this color scheme active fires appear bright red, burn scars appear brown, clouds appear white, and cloud shadows appear black. In Fig. 4 we show the relationship between band 3N and band 8 reflectance for the same scene. Several broad features are evident. First, there is a central cluster in which the band 3N and band 8 reflectances are largely uncorrelated but well constrained. This corresponds to vegetation, some soils, and burn scars. Next, there is an elongated cluster in which the reflectances are

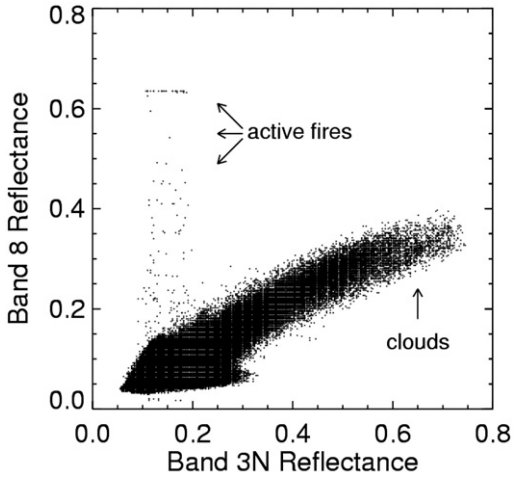

Fig. 4. Relationship between band 3N and band 8 top-of-atmosphere reflectance for all pixels comprising the scene shown in Fig. 3. For this particular scene, band 8 saturates at a reflectance of about 0.64.

very highly correlated, corresponding to clouds and, to a lesser extent, brighter soils. The third, vertically oriented cluster corresponds to pixels containing active fires. The apparent band 8 reflectance of these pixels is anomalously high due to the substantial emissive SWIR contribution from combustion. Overall, the reflectances of non-fire pixels are linearly related, and this relationship is sufficiently strong that the ratio of band 8 reflectance to band 3N reflectance is nearly constant. We will exploit this characteristic in developing a daytime fire detection algorithm for ASTER. Nighttime scenes, being devoid of reflected sunlight (barring a very small contribution from the Moon), are much less ambiguous, and active fires can be identified with thresholds applied to band 8 imagery.

4.2. Detection algorithm

For daytime scenes we use top-of-atmosphere reflectances computed for ASTER bands 3N and 8, denoted by ρ_3 and ρ_8, respectively. To produce compatible spatial resolutions, band 3N pixels are aggregated to 30 m spatial resolution by averaging. For nighttime scenes our approach requires the ASTER band 8 top-of-atmosphere radiance (L_8) only.

4.2.1. Daytime algorithm

In the following discussion we refer to the ratio (r) and the difference ($\Delta\rho$) of the band 3N and band 8 reflectances, where $r=\rho_8/\rho_3$ and $\Delta\rho=\rho_8-\rho_3$.

4.2.2. Step 1: mask obvious water pixels

Because our approach includes a contextual component in which local spatial statistics are computed, it is desirable to exclude water pixels during this process. Since ancillary water masks are currently unavailable at the scale of an ASTER pixel, we apply a simple band 8 threshold test on a per-pixel basis: all pixels for which $\rho_8<0.04$ are flagged as water and are excluded from further processing. While this value provided reasonably good identification of water pixels in our test scenes, it may need to be adjusted regionally to account for variations in, among other factors, depth, and the amount and type of suspended matter.

4.2.3. Step 2: identify obvious fire pixels

Pixels for which $r>2$ and $\Delta\rho>0.2$ are considered to be obvious fire pixels and are immediately flagged as containing an active fire. The difference test ensures that areas of exceptionally low reflectance are not incorrectly identified as a fire.

4.2.4. Step 3: identify candidate fire pixels

Pixels for which $r>1.1$ and $\Delta\rho>0.1$ that were not flagged as obvious fire pixels in the previous step are flagged as candidate fire pixels.

4.2.5. Step 4: background characterization

Neighboring pixels in a square window centered on the candidate fire pixel are used to estimate the mean non-fire "background" values of the reflectance ratio and band 8 reflectance. Pixels identified as obvious fire pixels in Step 2 are excluded from this window. Unlike the variable background windows used in contextual algorithms developed for coarser resolution (~1-km) sensors (e.g., Flasse and Ceccato, 1996; Giglio et al., 1999), the size of the background window is fixed at 61×61 pixels (1830 m×1830 m) in size. This scale, which was determined empirically, is reasonable given the much higher spatial resolution of ASTER. For small and moderate size fires, the majority of the 30-m pixels within a window of this size will be fire-free and usable for background characterization. On the other hand, the problematic case of the background window spanning a very large fire, and consequently leaving an insufficient number of non-fire pixels available for background characterization, will virtually never occur: most pixels within a very large fire will have already been identified as obvious fire pixels in Step 2, thus obviating the need for background characterization to be performed.

Four statistics are computed for pixels within the background window: the mean ($\overline{r}$) and standard deviation (σ_r) of the reflectance ratio, and the mean ($\overline{\rho_8}$) and standard deviation (σ_8) of the band 8 reflectance.

4.2.6. Step 5: contextual tests

For all candidate fire pixels the conditions

$$r>\overline{r}+\max(3\sigma_r, 0.5) \tag{4}$$

$$\rho_8>\overline{\rho_8}+\max(3\sigma_8, 0.05) \tag{5}$$

are evaluated, where $\max(u, v)$ denotes the larger of u and v. If both conditions are satisfied, the pixel is flagged as containing an active fire. Condition (4) is used to identify pixels exhibiting the anomalously high SWIR to VNIR ratio expected when an active fire is present in an ASTER pixel. Condition (5) is used to identify pixels having the anomalously high apparent SWIR reflectance caused by the presence of fires. It also prevents false alarms in pixels having an exceptionally low near-infrared reflectance but otherwise modest SWIR reflectance. This condition can occur, for example, within shallow, silt-laden water bodies. The minimum difference thresholds of 0.5 and 0.05 in Eqs. (4) and (5), respectively, prevent false alarms in unusually homogeneous regions.

4.2.7. Nighttime algorithm

The simplicity of nighttime scenes permit the use of a single band 8 radiance threshold. Pixels for which $L_8>1$ $Wm^{-2}sr^{-1}$ μm^{-1} are classified as fire pixels. This particular threshold value is roughly a factor of ten larger than the typical nighttime land surface radiance at 2.33 μm.

4.3. Expected performance

Although the daytime detection algorithm does not require saturation of band 8 to detect a fire, saturation is nevertheless a useful criterion for gauging the approximate fire detection capability of the instrument. As will be shown in Section 6, the majority of detected fires saturate band 8. Fig. 5 shows the minimum fire size that will reach the band-8 saturation level of 10.55 $Wm^{-2}sr^{-1}$ μm^{-1} (gain setting *normal*), indicating that ASTER can in principle detect flaming fires ~1 m^2 in size, and smoldering fires approximately 100 times larger.

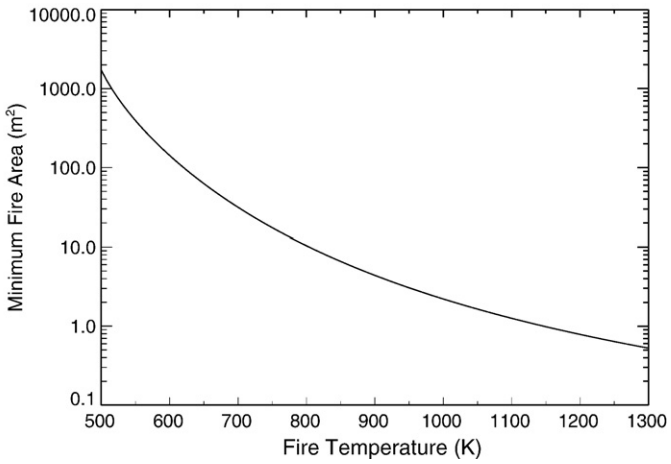

Fig. 5. Minimum fire size required to saturate ASTER band 8 (at normal gain) as a function of fire temperature under typical daytime conditions. A surface reflectance of 15% was assumed.

5. Algorithm evaluation

Of the 196 ASTER scenes used in this study, 96 were used for testing during algorithm development and the remaining 100 were set aside for algorithm evaluation. The evaluation scenes were partitioned into the following nine regions: Africa, Asia, Australia, India, Europe, Mexico, Russia, South America, and USA/Canada.

For each evaluation scene, manually identified fire pixels were stored in an "expert" fire mask. These masks were then compared to the fire masks generated by the detection algorithm, allowing the construction of error matrices which summarized algorithm performance for each region. The elements of the error matrix are shown in Tables 2 and 3.

A common measure of accuracy known as the *overall accuracy* is simply the ratio of the number of correctly classified pixels to the total number of pixels evaluated. In terms of the elements of the error matrix, the overall accuracy A is given by

$$A = \frac{M_{\mathrm{ff}} + M_{\mathrm{nn}}}{M_{\mathrm{ff}} + M_{\mathrm{fn}} + M_{\mathrm{nf}} + M_{\mathrm{nm}}}. \quad (6)$$

In the present work this metric is not particularly useful since the number of correctly classified non-fire pixels (M_{nn}) will generally dwarf all other elements of the error matrix. Eq. (6) will consequently nearly always uninformatively tell us that $A \approx 100\%$. Of more utility here is the *probability of detection* (P_{d}) and the *probability of false alarm* (P_{f}), where

$$P_{\mathrm{d}} = \frac{M_{\mathrm{ff}}}{M_{\mathrm{ff}} + M_{\mathrm{nf}}}. \quad (7)$$

and

$$P_{\mathrm{f}} = \frac{M_{\mathrm{fn}}}{M_{\mathrm{ff}} + M_{\mathrm{nn}}}. \quad (8)$$

The resulting probabilities computed using Eqs. (7) and (8) are presented in Table 4.

In most regions, P_d varied between 0.8 and 0.9, with a somewhat lower probability in Mexico ($P_{\mathrm{d}} = 0.71$). An unusually low probability of detection ($P_{\mathrm{d}} = 0.45$) was found for India. To help explain the poor performance in this region, we linked adjacent fire pixels within each expert fire mask into independent clusters, where each cluster was surrounded completely by either non-fire pixels or a scene edge. We next computed the median size of all fire-pixel clusters within each region (Table 4), and found that the smallest median cluster size occurred in India, where half of all fires identified were three 30-m ASTER pixels or less in size. This suggests that the fires in our Indian scenes are simply too small for reliable detection, a finding consistent with the fact that small agricultural-waste fires are abundant in this region.

False alarm probabilities varied between 9×10^{-8} (India) and 2×10^{-5} (USA/Canada). For a typical ASTER scene of ~5,000,000 30-m pixels, these extremes correspond to between less than 1 and 100 false fire pixels per scene. More representative intermediate false alarm rates ($P_{\mathrm{f}} \sim 5 \times 10^{-6}$) yield ~25 false fire pixels per scene. In an extension of our fire-pixel cluster analysis, we determined the fraction of false fire pixels connected to clusters of true fire pixels, f_c, and show this fraction in Table 4. In most regions the majority of false fire pixels were linked to clusters of true fire pixels, suggesting that most false fire pixels occur along the ambiguous fire boundaries.

Table 2
Elements of error matrix used to calculate accuracy measures

	Expert class	
Algorithm class	Fire	Non-fire
Fire	M_{ff}	M_{fn}
Non-fire	M_{nf}	M_{nn}

The first subscript denotes the class assigned to a pixel by the algorithm, and the second denotes the class assigned by the expert.

Table 3
Elements of error matrix for each region

Region	Scenes	M_{ff}	M_{nf}	M_{fn}	M_{nn}
Africa	19	4816	845	217	82,193,491
Australia	9	14255	2846	255	39,044,478
South America	10	4172	616	175	42,996,551
Mexico	10	1631	684	8	42,931,999
Europe	11	1372	147	282	47,401,479
India	10	2070	2507	4	43,240,339
USA/Canada	11	35160	8415	765	47,473,810
Russia	10	13548	2311	172	43,891,622
Southeast Asia	10	921	92	94	43,603,099

6. Fire characterization

6.1. Instantaneous fire temperature and area

A more extensive fire-product validation could be achieved if sub-pixel average fire temperatures and instantaneous fire areas were estimated using ASTER observations. This would permit fire detection probabilities to be established as a function of fire temperature and area, an appealing prospect as the resulting envelopes of detection are readily understandable. Temperature and area statistics would also allow more realistic fire scenes to be used in simulation-based approaches to validation (e.g., Dowty, 1996; Giglio et al., 1999, 2003). One approach is to use the bispectral method developed by Dozier (1981), which permits the retrieval of the temperature and area of a sub-pixel fire within an otherwise homogeneous pixel. Using slight modifications suggested by Giglio and Kendall (2001), we may write the total radiance L_i reaching the sensor in the ith band ($i = 1, 2$) as

$$L_i = \tau_i p B_i(T_{\mathrm{f}}) + (1 - p) L_{\mathrm{b},i}, \quad (9)$$

where T_{f} is the fire temperature, and p is the relative fraction of the pixel containing the fire. The factor τ_i is the band-averaged atmospheric transmittance, weighted by the spectral response of the ith channel, and $B_i(T_{\mathrm{f}})$ is the band-averaged Planck function. The quantities $L_{\mathrm{b},1}$ and $L_{\mathrm{b},2}$ are independent estimates of the radiance contributions from the non-fire portion (or background) of the target pixel, usually taken as the radiances of a neighboring, non-fire pixel, or

Table 4
Regional accuracy measures for ASTER fire detection algorithm, including the probability of detection (P_{d}), probability of false alarm (P_{f}), and the fraction of false fire pixels connected to clusters of true fire pixels (f_c)

Region	P_{d}	P_{f}	Median Cluster Size	f_c
Africa	0.85	3×10^{-6}	4.0	0.83
Australia	0.84	8×10^{-6}	6.0	0.93
South America	0.87	4×10^{-6}	4.0	0.92
Mexico	0.71	2×10^{-7}	4.0	0.25
Europe	0.90	6×10^{-6}	4.0	0.82
India	0.45	9×10^{-8}	3.0	1.0
USA/Canada	0.81	2×10^{-5}	5.0	0.64
Russia	0.85	4×10^{-6}	5.0	0.92
Southeast Asia	0.91	2×10^{-6}	3.5	0.76

the average radiances of several neighboring, non-fire pixels. Given these estimates, Eq. (9) may be solved numerically for p and T_f. An important assumption built into Eq. (9) is that the fire radiates as a true black body, and thus has unit emissivity. The impact of a grey-body fire fraction is considered by Giglio and Kendall (2001).

There are numerous well documented limitations of the bispectral approach for fire characterization (e.g., Langaas, 1993; Giglio and Kendall, 2001; Shephard and Kennelly, 2003). With respect to the ASTER instrument, there are several limitations of particular significance. First, it is difficult to obtain a good estimate of the background radiance ($L_{b,i}$) within a fire pixel since the non-fire fraction contains hot, recently-burned areas having a unique temperature and area distribution not matched in neighboring non-fire pixels. This is especially true at the scale of an ASTER pixel: fire heterogeneity is more pronounced compared to sensors having ~1 km spatial resolution (or coarser) most often used for operational fire monitoring. Second, only a tiny fraction of ASTER scenes have been acquired with even a subset of the SWIR bands in one of the low gain modes, making saturation of these bands extremely common when observing fires. Since the bispectral method cannot be applied when one or both bands saturate, one might potentially appeal to "band hopping", where the band-pair used to solve Eq. (9) is independently chosen from the pool of unsaturated channels for each fire pixel. However, except for the case of homogeneous fires, solving Eq. (9) with different band combinations can yield dramatically different solutions for p and T_f. As discussed by Giglio and Justice (2003), this phenomenon arises because the bispectral method models fires as having a single, homogeneous temperature, when in fact they have a more complicated temperature distribution. In general, a fire model should allow at least a hotter flaming and a cooler smoldering component. While multiple-component models have been used successfully with hyperspectral instruments (Green, 1996; Dennison et al., 2006), a two-fire-temperature model would require a minimum of four unsaturated ASTER channels, a feat bordering on the miraculous for nearly all of the ASTER scenes that have been acquired to date. Finally, band-to-band coregistration must meet fairly stringent requirements for the retrieved fire parameters to be accurate for fires occupying a small fraction of the pixel (Shephard and Kennelly, 2003). A practical method of reducing the impact of misregistration (at the cost of spatial resolution) is to apply the bispectral method to clusters of adjacent fire pixels (Oertel et al., 2003; Zhukov et al., 2006), where the radiances L_1 and L_2 in Eq. (9) become averages of all pixels within the cluster.

Given the above difficulties, and based on initial unsuccessful tests with several ASTER scenes, we did not pursue the retrieval of fire temperature and area from ASTER observations. Instead, we direct our efforts toward retrieval of fire radiative power, a remotely-sensed measure of fire intensity of growing interest.

6.2. Fire radiative power

The MODIS active fire product includes an estimate of the fire radiative power (FRP) emitted within each MODIS pixel (Kaufman et al., 1998). As originally conceived, the FRP, when integrated over time, can be used to estimate combusted biomass, and is thus a topic of current research for its potential in quantifying pyrogenic greenhouse-gas emissions (e.g., Ichoku & Kaufman, 2005). Subsequent work has extended the scope of potential applications to include the discrimination of different fire types (Wooster & Zhang, 2004; Smith & Wooster, 2005) and the estimation of smoke injection height (Mazzoni et al., 2007). Although some validation of the MODIS FRP has already been performed (Wooster, 2002; Wooster et al., 2003), such cases are few in number and not yet globally representative. There is interest, therefore, in validating the MODIS FRP using comparatively large samples of ASTER fire scenes. Here we briefly consider the feasibility of such a task.

The FRP for N different fire components within a pixel, each having its own temperature and area, is defined as (Wooster et al., 2003)

$$\mathrm{FRP} = A_{\mathrm{pix}}\epsilon\sigma\sum_{i=1}^{N} p_i T_i^4, \tag{10}$$

where p_i is the fraction of the pixel occupied by the ith fire component with temperature T_i, A_{pix} is the area of the pixel, ϵ is the weighted mean emissivity of the fire components, and σ is the Stefan-Boltzmann constant. For the special case of a wavelength near 4 μm, Wooster et al. (2003) showed that FRP could be remotely sensed using a single middle-infrared band via the relationship

$$\mathrm{FRP} \approx \frac{A_{\mathrm{pix}}\epsilon\sigma}{a\epsilon_{\mathrm{MIR}}}(L - L_b), \tag{11}$$

where L is the 4 μm radiance of a fire pixel, L_b is an independent estimate of the radiance contributed by the non-fire portion of the pixel, ϵ_{MIR} is the middle-infrared fire emissivity, and a is a constant. This unique property of the middle-infrared was first noted by Kaufman et al. (1998), who derived an empirical relationship relating the FRP to brightness temperature.

Since Eq. (11) is not applicable to the bands available on ASTER, an alternative approach might be to use the instantaneous fire temperature and sub-pixel area estimates obtained from Eq. (9) to calculate the FRP directly, i.e.,

$$\mathrm{FRP} = A_{\mathrm{pix}}\epsilon\sigma p T_f. \tag{12}$$

Use of Eq. (12) brings with it all of the limitations inherent in the bispectral technique, and we consequently did not attempt to apply such an approach to the ASTER scenes used in our analysis. Motivated by the fact that the ASTER bands weight the flaming and smoldering contributions differently, we instead seek an empirical relationship which expresses the FRP as a linear combination of the "surplus radiance" observed in $n \geq 1$ ASTER bands, i.e.,

$$\mathrm{FRP} = \sum_{j=1}^{n} c_j(L_j - L_{b,j}), \tag{13}$$

where L_j is the observed radiance in band j for a fire pixel, $L_{b,j}$ is an independent estimate of the non-fire background radiance, and c_j is a band-specific constant. Here, L_j and $L_{b,j}$ are bottom-of-atmosphere radiances since we can make use of the ASTER atmospherically-corrected SWIR Surface Reflectance product (AST 07S, AST 07XTS) and TIR Surface Radiance product (AST 09T) when attempting fire characterization.

The constants appearing in Eq. (13) were calculated for different band combinations by means of a simple fire model in which bottom-of-atmosphere radiances were computed for 120,000 simulated fires. Each fire was assigned independent flaming and smoldering components having temperatures ranging from 750–1200 K and 500–700 K, respectively, drawn randomly from uniform distributions. The area of each flaming and smoldering component was also assigned randomly for each simulated fire, with the constraint that the total fire area (flaming and smoldering combined) occupied no more than 90% of an ASTER pixel. The emissivity of the non-fire component within each pixel was randomly selected from the interval [0.97,0.99], and unit fire emissivity was assumed.

An initial analysis revealed that a minimum of four independent SWIR bands were required to match the accuracy that could be achieved using only three TIR channels. For this reason, as well as the scarcity of ASTER scenes having a consistent set of unsaturated SWIR bands for fire pixels, we restricted the remainder of our analysis to the TIR bands. Within this restricted wavelength interval, highest accuracy is attained by spacing the bands sufficiently far apart such

that the Planck function yields significantly different radiances at a given fire temperature. We therefore opted to use bands 10, 12, and 14 in Eq. (13). Our empirical relationship is then

$$\mathrm{FRP} = c_{10}(L_{10} - L_{\mathrm{b},10}) + c_{12}(L_{12} - L_{\mathrm{b},12}) + c_{14}(L_{14} - L_{\mathrm{b},14}). \quad (14)$$

By regressing the true FRP of 200,000 simulated fires against the corresponding surplus radiance in bands 10, 12, and 14, we obtained values for the coefficients of $c_{10}=9.98\pm0.06$ MW W^{-1} m^2 sr μm, $c_{12}=-14.6\pm0.1$ MW W^{-1} m^2 sr μm, and $c_{14}=4.85\pm0.08$ MW W^{-1} m^2 sr μm. Fig. 6 shows the FRP retrieved using Eq. (14) versus the true FRP for a random subset of the simulated fires.

We note that Eq. (14) can be applied on either a per-fire-pixel or a per-fire-pixel-cluster basis. For validation purposes the latter is generally most appropriate as it minimizes the effects of geolocation error and the inherent imprecision of pixel boundaries. In this case, L_j represents the mean band j radiance for a contiguous cluster of 90-m TIR pixels which contain one or more fire pixels identified in the 30-m fire mask. When computing the average radiances for each cluster, the individual TIR radiance of each pixel should then be weighted by the number of 30-m fire pixels contained within it.

Denoting the uncertainties in the fit coefficients, the radiance of each fire pixel (or cluster of pixels), and the background radiance estimate as Δc_j, ΔL_j, and $\Delta L_{\mathrm{b},j}$, respectively, and assuming the uncertainties are both independent and random, the net uncertainty in retrieved FRP is given by

$$\begin{aligned}\Delta\mathrm{FRP} &= \left(\sum_j\left[\left(\frac{\partial\mathrm{FRP}}{\partial c_j}\Delta c_j\right)^2+\left(\frac{\partial\mathrm{FRP}}{\partial L_j}\Delta L_j\right)^2+\left(\frac{\partial\mathrm{FRP}}{\partial L_{\mathrm{b},j}}\Delta L_{\mathrm{b},j}\right)^2\right]\right)^{1/2}\\ &= \left(\sum_j\left[\left((L_j-L_{\mathrm{b},j})\Delta c_j\right)^2+\left(c_j\Delta L_j\right)^2+\left(c_j\Delta L_{\mathrm{b},j}\right)^2\right]\right)^{1/2},\end{aligned} \quad (15)$$

where the index $j=\{10,12,14\}$. Note that in Eq. (15) the quantities ΔL_j and $\Delta L_{\mathrm{b},j}$ represent the combined uncertainty in radiance from instrument noise, quantization, and the atmospheric correction.

6.3. Evaluation of retrieved fire radiative power

We evaluated the empirical FRP relationship in Eq. (14) using four prescribed fires set in Szendrő, Hungary on 3 September 2005 which were active at the time of the descending (daytime) Terra overpass. We scheduled a simultaneous ASTER scene acquisition with a SWIR-band gain setting of *low-2*, but due to a scheduling error a gain of *normal* was inadvertently used. While this had no impact on the TIR channels (all of which remained unsaturated), it did result in saturation of many of the SWIR pixels overlapping fires. Fuel (straw and, in one case, a rubber tire) was arranged and ignited so as to match, as closely as possible, a range of pre-specified flaming areas at the time of the Terra overpass. Within several minutes of the overpass, the maximum instantaneous fire temperature was estimated for each fire using multiple FLIR Systems handheld thermal radiometers (models ThermaCAM E45, InfraCAM, and ThermaCAM P65), which acquired real-time imagery at an effective spatial resolution of ~10 cm. Fire characteristics are summarized in Table 5, with the FRP calculated using the observed maximum fire temperature as a proxy for the mean fire temperature. This was not entirely unreasonable for the three smallest fires since their temperature fields were observed to be relatively homogeneous. The temperature field of the 500 m^2 fire was noticeably heterogeneous, however, hence the recorded maximum is consequently less representative of the mean fire temperature, and the FRP calculated for this fire will overestimate the true FRP. We will return to this issue momentarily.

Table 5
Fire characteristics of prescribed fires for which quantitative ground-based estimates were available at the time of the Terra overpass

Fuel	Area (m^2)	Maximum Temperature (K)	FRP (MW)
Straw	50	661	0.54
Straw	100	693	1.31
Straw	500	693	6.54
Tire	10	1166	1.05

Fig. 7 shows the FRP retrieved for each cluster of fire pixels (each of which corresponds to a single prescribed fire) versus the FRP estimated from our ground-truth data. For the 50 m^2 and 100 m^2 straw fires the retrieved and ground truth values are in good agreement. The bulk of the underestimation in retrieved FRP for the 500 m^2 fire (by about 17%) most likely reflects the fact that, as mentioned above, we calculated our ground-truth FRP estimates using the maximum fire temperature (which was readily measurable) rather than the mean fire temperature (which was not readily measurable). Clearly this will overestimate our ground-based FRP estimate. Working backwards, we calculated that the retrieved and ground-based estimates would be in agreement for a fire temperature of 662 K, a value consistent with the ~50 K variation in temperature observed over the combustion zone at the time of the Terra overpass. Finally,

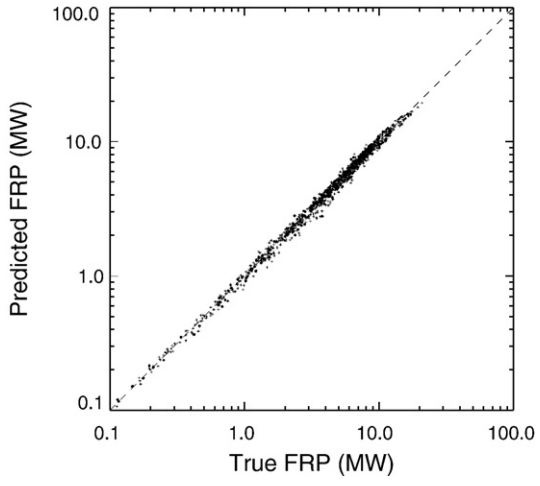

Fig. 6. Predicted FRP (via Eq. (14)) versus true FRP for 1000 simulated fires. Dashed line indicates perfect agreement.

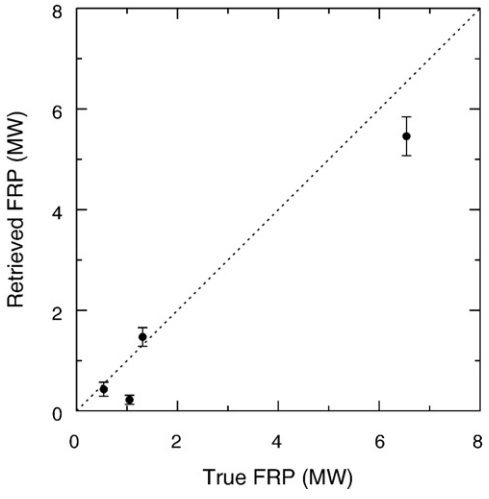

Fig. 7. Retrieved mean FRP versus FRP calculated from ground truth data collected for prescribed burns. Dashed line indicates perfect agreement.

agreement for the 10 m^2 fire was poor, with the true FRP underestimated by nearly 80%. We suspect that the heavy soot associated with this fire (a burning tire) was primarily responsible for the poor agreement in this case. In addition to reducing the apparent radiance of the fire as measured by the sensor through absorption, heavy aerosol loadings are likely to substantially degrade the quality of the atmospheric correction.

We note that this exercise represents a first step toward a proper validation of our ASTER FRP retrieval using contemporaneous ground-based measurements. Among other requirements, rigorous validation would include precise measurements of fire temperature, with consideration of the differences between satellite and ground viewing geometries, obviously for a much larger sample of fires. Nevertheless, our preliminary evaluation indicates relatively good agreement for three of the four fires considered in this study.

7. Conclusion

We have presented an automated fire detection algorithm for the ASTER sensor capable of mapping actively burning fires at 30-m spatial resolution. For daytime scenes, our approach uses band 8 (2.33 μm) and band 3N (0.82 μm) reflectance imagery. The former is sensitive to black-body radiation emitted by fires, while the latter is insensitive to such radiation but that provides a highly-correlated reflectance over "normal" (non-fire) components of terrestrial scenes. For nighttime scenes a simple 2.33-μm radiance threshold is applied.

Based on a statistical analysis of 100 ASTER scenes, we established omission and commission error rates for nine different regions. In most regions, the probability of detection varied between 0.8 and 0.9, with a somewhat lower probability in Mexico ($P_d = 0.71$). An unusually low probability of detection ($P_d = 0.45$) was found for India, most likely because the fires in our Indian scenes were too small for reliable detection, a finding consistent with the fact that small agricultural-waste fires are abundant in this region. Probabilities of false alarm varied between 9×10^{-8} (India) and 2×10^{-5} (USA/Canada). In most regions, the majority of false fire pixels were linked to clusters of true fire pixels, suggesting that most false fire pixels occur along the ambiguous fire boundaries.

With respect to fire characterization, we formulated an empirical method for estimating fire radiative power using three ASTER thermal infrared channels. A preliminary evaluation of this approach using four prescribed fires demonstrated that retrieved values were accurate to within 20%, with the exception of one fire partially obscured by heavy soot.

Despite difficulty in demarcating precise boundaries of large fire fronts due to saturation-induced pixel blooming, fire maps derived from ASTER are an important tool for the validation of the Terra MODIS active fire products. The use of ASTER fire masks for the validation of other fire monitoring sensors is also possible provided the sensor resides on a satellite having at least an occasional overpass coincident (or nearly coincident) with the Terra satellite. Sensors meeting this criterion include the Tropical Rainfall Measuring Mission (TRMM) VIRS, the GOES Imager, and SEVIRI on board Meteosat 8 and 9. Validation is perhaps the most important application of ASTER in the context of fire monitoring as the sensor's spatial coverage and revisit frequency limit its utility for routine fire monitoring. Other applications include studies of the fine structure of fire fronts, and the spatial structure of burn scars and the associated combustion completeness.

Acknowledgements

We thank Simon Hook (Jet Propulsion Laboratory) and two anonymous reviewers for helpful comments and technical suggestions. Funding for this work was provided through NASA's Earth Observing System and Phase III Large-scale Biosphere-Atmosphere Experiment in Amazonia (LBA) programs.

References

Arino, O. & Rosaz, J. M. (1999, June). 1997 and 1998 world ATSR fire atlas using ERS-2 ATSR-2 data. In L. F. Neuenschwander, K. C. Ryan, & G. E. Golberg (Eds.), *Proceedings of the Joint Fire Science Conference. University of Idaho and the International Association of Wildland Fire, Boise, Idaho,* (pp. 177–182).

Csiszar, I., Morisette, J., & Giglio, L. (2006). Validation of active fire detection from moderate resolution satellite sensors: The MODIS example in Northern Eurasia. *IEEE Transactions on Geoscience and Remote Sensing, 44*, 1757–1764.

Dennison, P. E., Charoensiri, K., Roberts, D. A., Peterson, S. H., & Green, R. O. (2006). Wildfire temperature and land cover modeling using hyperspectral data. *Remote Sensing of Environment*, *100*, 212–222.

Dowty, P. R. (1996). The simulation of AVHRR data for the evaluation of fire detection techniques. In J. S. Levine (Ed.), *Biomass burning and global change: Remote sensing, modeling and inventory development, and biomass burning in Africa*, *Vol. 1* (pp. 40–50). Cambridge: MIT Press.

Dozier, J. (1981). A method for satellite identification of surface temperature fields of subpixel resolution. *Remote Sensing of Environment*, *11*, 221–229.

Elvidge, C. D., Kroehl, H. W., Kihn, E. A., Baugh, K. E., Davis, E. R., & Hao, W. M. (1996). Algorithm for the retrieval of fire pixels from DMSP operational linescan system data. In J. S. Levine (Ed.), *Biomass burning and global change: Remote sensing, modeling and inventory development, and biomass burning in Africa*, *Vol. 1* (pp. 73–85). Cambridge: MIT Press.

Flasse, S. P. & Ceccato, P. (1996). A contextual algorithm for AVHRR fire detection. *International Journal of Remote Sensing, 17*, 419–424.

Giglio, L. & Justice, C. O. (2003). Effect of wavelength selection on characterization of fire size and temperature. *International Journal of Remote Sensing, 24*(17), 3515–3520.

Giglio, L. & Kendall, J. D. (2001). Application of the dozier retrieval to wildfire characterization: A sensitivity analysis. *Remote Sensing of Environment*, *77*, 34–39.

Giglio, L. Kendall, J. D., & Justice, C. O. (1999). Evaluation of global fire detection algorithms using simulated AVHRR infrared data. *International Journal of Remote Sensing, 20*(10), 1947–1985.

Giglio, L., Kendall, J. D., & Mack, R. (2003). A multi-year active fire data set for the tropics derived from the TRMM VIRS. *International Journal of Remote Sensing*, *24*(22), 4505–4525.

Green, R. O. (1996). Estimation of biomass fire temperature and areal extent from calibrated AVIRIS spectra. *Summaries of the Sixth Annual JPL Airborne Earth Science Workshop* (pp. 105–113). Pasadena: JPL Publication 96-4.

Ichoku, C. & Kaufman, Y. J. (2005). A method to derive smoke emission rates from MODIS fire radiative energy measurements. *IEEE Transactions on Geoscience and Remote Sensing*, *43*, 2636–2649.

Ichoku, C., Kaufman, Y. J., Giglio, L., Li, Z., Fraser, R. H., Jin, J. Z. & Park, W. M. (2003). Comparative analysis of daytime fire detection algorithms using AVHRR data for the 1995 fire season in Canada: Perspective for MODIS. *International Journal of Remote Sensing*, *24*, 1669–1690.

Iwasaki, A., Fujisada, H., Akao, H., Shindou, O., & Akagi, S. (2002). Enhancement of spectral separation performance for ASTER/SWIR.. In M. Strojnik, & B. F. Andresen (Eds.), *Infrared Spaceborne Remote Sensing, Vol. 4486* (pp. 42–50). SPIE IX.

Justice, C. O., Giglio, L., Korontzi, S., Owens, J., Morisette, J. T., Roy, D., Descloitres, J. Alleaume, S., Petitcolin, F., & Kaufman, Y. (2002). The MODIS fire products. *Remote Sensing of Environment*, *83*, 244–262.

Justice, C. O., Kendall, J. D., Dowty, P. R., & Scholes, R. J. (1996). Satellite remote sensing of fires during the SAFARI campaign using NOAA AVHRR data. *Journal of Geophysical Research*, *101*(D23), 23851–23863.

Kaufman, Y. J., Justice, C. O., Flynn, L. P., Kendall, J. D., Prins, E. M., Giglio, L., Ward, D. E., Menzel, W. P., & Setzer, A. W. (1998). Potential global fire monitoring from EOS-MODIS. *Journal of Geophysical Research*, *103*(D24), 32215–32238.

Langaas, S. (1993). A parameterised bispectral model for savanna fire detection using AVHRR night images. *International Journal of Remote Sensing, 14*, 2245–2262.

Li, Z. Kaufman, Y. J. Ichoku, C. Fraser, R. Trishchenko, A. Giglio, L., et al. (2001). A review of AVHRR-based active fire detection algorithms: principles, limitation, and recommendations. In F. J. Ahern, J. G. Goldammer, & C. O. Justice (Eds.), *Global and Regional Vegetation Monitoring from Space: Planning a Coordinated International Effort* (pp. 199–225). The Hague: SPB Academic Publishing.

Mazzoni, D., Logan, J. A., Diner, D., Kahn, R., Tong, L., & Li, Q. (2007). A data-mining approach to associating MISR smoke plume heights with MODIS fire measurements. *Remote Sensing of Environment*, *107*, 138–148.

Morisette, J. T., Giglio, L., Csiszar, I., & Justice, C. O. (2005). Validation of the MODIS active fire product over Southern Africa with ASTER data. *International Journal of Remote Sensing*, *26*, 4239–4264.

Morisette, J. T., Giglio, L., Csiszar, I., Setzer, A., Schroeder, W., Morton, D., & Justice, C. O. (2005). Validation of MODIS active fire detection products derived from two algorithms. *Earth Interactions*, *9*(9), 1–25.

Oertel, D., Briess, K., Halle, W., Neidhardt, M., Lorenz, E., Sandau, R., et al. (2003). Airborne forest fire mapping with an adaptive infrared sensor. *International Journal of Remote Sensing*, *24*, 3663–3682.

Prins, E. M., Schmetz, J., Flynn, L. P., Hillger, D. W., & Feltz, J. M. (2001). An overview of diurnal active fire monitoring using a suite of international geostationary satellites. In F. J. Ahern, J. G. Goldammer, & C. O. Justice (Eds.), *Global and Regional Vegetation Monitoring from Space: Planning a Coordinated International Effort* (pp. 145–170). The Hague: SPB Academic Publishing.

Roberts, G. & Wooster, M. J. (2007). New perspectives on African biomass burning dynamics. *EOS*, *88*(38), 369–370.

Shephard, M. W. & Kennelly, E. J. (2003). Effect of band-to-band coregistration on fire property retrievals. *IEEE Transactions on Geoscience and Remote Sensing*, *41*, 2648–2661.

Smith, A. M. S. & Wooster, M. J. (2005). Remote classification of head and backfire types from MODIS fire radiative power observations. *International Journal of Wildland Fire*, *14*, 249–254.

Stroppiana, D., Pinnock, S. & Grégoire, J. M. (2000). The Global Fire Product: Daily fire occurrence from April 1992 to December 1993 derived from NOAA AVHRR data. *International Journal of Remote Sensing*, *21*, 1279–1288.

Wooster, M. J. (2002). Small-scale experimental testing of fire radiative energy for quantifying mass combusted in natural vegetation fires. *Geophysical Research Letters*, *29*(21), 2027.

Wooster, M. J. & Zhang, Y. H. (2004). Boreal forest fires burn less intensely in Russia than in North America. *Geophysical Research Letters*, *31*, L20505.

Wooster, M. J., Zhukov, B., & Oertel, D. (2003). Fire radiative energy for quantitative study of biomass burning: derivation from the BIRD experimental satellite and comparison to MODIS fire products. *Remote Sensing of Environment*, *86*, 83–107.

Yamaguchi, Y., Kahle, A. B., Tsu, H., Kawakami, T., & Pniel, M. (1998). Overview of Advanced Spaceborne Thermal Emission and Reflection Radiometer (ASTER). *IEEE Transactions on Geoscience and Remote Sensing*, *46*, 1062–1071.

Zhukov, B., Lorenz, E., Oertel, D., Wooster, M., & Roberts, G. (2006). Spaceborne detection and characterization of fires during the bi-spectral infrared detection (BIRD) experimental small satellite mission (2001–2004). *Remote Sensing of Environment*, *100*, 29–51.